1   Revision 3

2   # Chenmingite, $FeCr_2O_4$ in the $CaFe_2O_4$-type structure, a shock-induced,

3   # high-pressure mineral in the Tissint Martian meteorite

4

5   Chi Ma[1,*], Oliver Tschauner[2], John R. Beckett[1], Yang Liu[3], Eran Greenberg[4], Vitali B.
6   Prakapenka[4]

7

8   [1]Division of Geological and Planetary Sciences, California Institute of Technology,

9   Pasadena, CA 91125, USA

10   [2]Department of Geoscience, University of Nevada, Las Vegas, NV 89154, USA

11   [3]Jet Propulsion Laboratory, California Institute of Technology, Pasadena, CA 91109, USA

12   [4]GSECARS, University of Chicago, Argonne National Laboratory, Chicago, IL 60637, USA

13

14   **ABSTRACT**

15   Chenmingite ($FeCr_2O_4$; IMA 2017-036), is a high-pressure mineral,

16   occurring as micrometer to submicrometer-sized lamellae within precursor

17   chromite grains along with xieite and Fe,Cr-rich ulvöspinel next to shock-induced

18   melt pockets, from the Tissint Martian meteorite. The composition of type

19   chenmingite by electron probe analysis shows an empirical formula of

20    $(Fe^{2+}_{0.75}Mg_{0.23}Mn_{0.02})(Cr_{1.60}Al_{0.29}Fe^{3+}_{0.06}Fe^{2+}_{0.04}Ti_{0.02})_{\Sigma2.01}O_4$. The general and

21   end-member formulas are $(Fe,Mg)(Cr,Al)_2O_4$ and $FeCr_2O_4$. Synchrotron X-ray

22   diffraction reveals that chenmingite has an orthorhombic *Pnma* $CaFe_2O_4$-type

23   (CF) structure with unit cell dimensions: $a = 9.715(6)$ Å, $b = 2.87 (1)$ Å, $c = 9.49$

24   (7) Å, $V = 264.6 (4)$ Å, and $Z = 4$. Both chenmingite and xieite formed by solid

25   state transformation of precursor chromite under high pressure and high

26   temperature during the Tissint impact event on Mars. The xieite regions are

27   always in contact with melt pockets, whereas chenmingite lamellae only occur

28   within chromite, a few micrometers away from the melt pockets. This

29   arrangement suggests that chenmingite formed under similar pressures as xieite

30   but at lower temperatures, in agreement with experimental studies.

31

32   **Keywords**: Chenmingite, $FeCr_2O_4$, high-pressure mineral, shock-induced phase, Tissint

33   Martian meteorite, shergottite.

34   *E-mail: chi@gps.caltech.edu

35

36   **INTRODUCTION**

37   The Tissint Martian meteorite is a fresh, highly-shocked, olivine-phyric shergottite

38   (e.g., Baziotis et al. 2013; Ma et al. 2015, 2016). Around shock-generated melt pockets and

39   veins in this meteorite, olivine is often transformed to ringwoodite or ahrensite and, in the

40   immediate vicinity of the melt veins or pockets, to bridgmanite plus wüstite (Ma et al. 2016).

41   Plagioclase is transformed to maskelynite, locally melted and partially crystallized to

42   tissintite (Ma et al. 2015) and zagamiite-stishovite assemblages. These responses to shock

43   conditions on Mars provide clues to the nature of the ejection events for Martian meteorites

44   and to local shock conditions. Novel high-pressure minerals can narrow constraints on shock

45   metamorphism in meteorites and the scale of impact events on their parent bodies. As natural

46   phases, they contain minor chemical components which can guide experimental research

47   about deep mantle mineralogy and provide constraints in assessing chemical or textural

48   signatures that survive retrograde transformation in ultrahigh pressure terrains.

49   Here, we describe a new high-pressure mineral chenmingite, $FeCr_2O_4$ with a *Pnma*

50   orthorhombic $CaFe_2O_4$-type (CF) structure. It occurs in Tissint within chromite grains in

51   contact with shock melt pockets (Fig. 1). Chen et al. (2003a) first reported $FeCr_2O_4$-CF in the

52   Suizhou meteorite along with xieite but did not name this phase. It has also been synthesized

53   at high pressures and moderate temperatures (e.g., Chen et al. 2003a; Ishii et al. 2014).

54   Preliminary results of this work were given by Ma et al. (2018).

55   The mineral chenmingite ($FeCr_2O_4$; IMA 2017-036) has been approved by the

56   Commission on New Minerals, Nomenclature and Classification of the International

57   Mineralogical Association (Ma and Tschauner 2017). It is one of thirteen newly-approved

58   high-pressure minerals discovered in shocked meteorites since 2013 (Ma 2018). The name is

59   in honor of Ming Chen, a cosmochemist and mineralogist at the Guangzhou Institute of

60   Geochemistry, Chinese Academy of Sciences, for his outstanding contributions to research

61   on high-pressure mineralogy of meteorites, shock metamorphism and terrestrial impact

62   craters. Among his contributions is the discovery of natural $FeCr_2O_4$ with a CF structure and

2

63   xieite (the natural $CaTi_2O_4$-type polymorph of chromite) in the Suizhou meteorite, a highly

64   shocked L6 chondrite (Chen et al. 2003a, b; 2008).

65

66   <div align="center">**SAMPLE AND ANALYTICAL METHODS**</div>

67   The Tissint meteorite, which fell at Tata, Morocco on 18 July 2011, is a Martian

68   meteorite (olivine-phyric shergottite). The type material is in Tissint section UT2 deposited in

69   the Meteorite Collection of the Frank H. McClung Museum at the University of Tennessee,

70   Knoxville, Tennessee 37996, USA. Section UT2 also hosts type ahrensite (IMA 2013-028;

71   Ma et al. 2016) and type tissintite (IMA 2013-027; Ma et al. 2015). Tissint consists mostly of

72   olivine (microphenocrysts and magnesian macrocrysts with thin ferroan rims), pyroxene

73   (mostly pigeonite with some subcalcic augites), maskelynite (An58-69), with minor chromite

74   and ilmenite, and accessory pyrrhotite, merrillite and magnetite. The meteorite contains

75   scattered shock melt pockets and rare melt veins, and associated high pressure phases.

76   High-resolution scanning electron microscope (SEM), electron back-scatter

77   diffraction (EBSD), electron probe microanalysis (EPMA), and synchrotron X-ray diffraction

78   (SXRD) were used to characterize the composition, structure and petrography of chenmingite

79   and associated phases. Back-scatter electron (BSE) imaging was performed using a ZEISS

80   1550VP field emission SEM. EBSD analyses were attempted using an HKL EBSD system on

81   a ZEISS 1550VP SEM, operated at 20 kV and 6 nA in focused-beam mode with a 70º tilted

82   stage and variable pressure mode (25 Pa). However, no meaningful EBSD pattern was

83   obtained from chenmingite. Chemical analyses of chenmingite and associated phases were

84   carried out using a JEOL 8200 electron microprobe interfaced with the Probe for EPMA

85   program from Probe Software, Inc. and operated in focused beam mode at 15 kV and 15 nA

86   with a probe diameter of ~150 nm. Standards were chromite ($CrK\alpha$, $FeK\alpha$), spinel ($AlK\alpha$,

87     $MgK\alpha$), TiO_2 ($TiK\alpha$), and Mn_2SiO_4 ($MnK\alpha$). Quantitative elemental microanalyses were

88   processed with the CITZAF correction procedure (Armstrong 1995) and analytical results are

89   given in Table 1.

90   Synchrotron diffraction data were collected at the undulator beamline 13-IDD

91   (GSECARS, APS, Argonne National Laboratory) using a primary beam of wavelength

92   0.495936 Å, monochromatized by a double-crystal Si monochromator. The X-ray beam was

93   focused to 2×3 μm^2 by vertical and horizontal Kirkpatrick-Baez mirrors of 200 mm focal

94   length. A MAR165 CCD area detector was used for collecting diffraction data, which were

3

95   obtained in forward scattering geometry. Calibration was conducted with GSE-ADA (Dera et

96   al. 2013) and DIOPTAS (Prescher and Prakapenka 2015). Integration and correction for

97   geometric distortion were conducted with DIOPTAS (Prescher and Prakapenka 2015).

98   Diffraction from chenmingite is prominent in some locations but generally overlaps with

99   xieite, host chromite, and ulvöspinel. A pattern from the border of a melt pocket (Fig. 2) that

100   contains no signal from xieite and comparatively weak diffraction from chromite was used

101   for structure modeling.

102

103   **RESULTS**

104   **Occurrence, appearance, physical and optical properties**

105   In Tissint, type chenmingite occurs in the interior of two chromite grains exposed to

106   melt pockets (Fig. 1). Xieite ($FeCr_2O_4$ in a $CaTi_2O_4$-type (CT) structure; e.g., Chen et al.

107   2008) and Fe,Cr-rich ulvöspinel occur in the same precursor chromite grains but these phases

108   are in direct contact with shock melt pockets (Fig. 1), whereas chenmingite lamellae only

109   occur within the precursor chromite, a few micrometers away from the melt pockets. The

110   shock melt pockets, surrounded by olivine (Fo42-73), pyroxene and 'maskelynite' (An64-

111   66), contain abundant ringwoodite-ahrensite, bridgmanite and wüstite transformed from

112   olivine, and tissintite in maskelynite, and clinopyroxene from relict pyroxene or the melt.

113   Chenmingite occurs as lamellae, < 1 µm in width and up to 4 µm in length, set in

114   arrays within the host chromite (Fig. 1c). It is optically not distinguishable from chromite.

115   Higher scratching hardness than chromite is evidenced by disruption of polishing streaks as

116   they cross chenmingite lamellae. Streak, tenacity, cleavage, fracture and reflection

117   pleochroism could not be determined empirically because of the small grain size. The

118   density, calculated from its crystal structure and the empirical formula, as described below, is

119   5.27 ±0.02 g/cm^3.

120   **Chemical composition and crystallography**

121   The composition (Table 1) of type chenmingite corresponds to an empirical formula

122   based on 3 cations and 4 oxygens *apfu* of ($Fe^{2+}_{0.75}Mg_{0.23}Mn_{0.02}$)

123   ($Cr_{1.60}Al_{0.29}Fe^{3+}_{0.06}Fe^{2+}_{0.04}Ti_{0.02}$)$_{\Sigma2.01}O_4$, where Fe^{2+}/ Fe^{3+} was obtained by assuming an M_3O_4

124   stoichiometry. Within 1-σ uncertainties, the composition of chenmingite is the same as that

125   of host chromite as well as that of xieite from the same host grain (Table 1). Chenmingite has

126   a general formula of $(Fe,Mg)(Cr,Al)_2O_4$ and an end-member formula of $FeCr_2O_4$. The Fe,Cr-

4

127   rich ulvöspinel, as indicated by EBSD and synchrotron diffraction, has an empirical formula

128   of $(Fe^{2+}_{0.86}Mg_{0.12}Mn_{0.02})(Cr_{0.57}Fe^{3+}_{0.31}Al_{0.23}Ti_{0.44}Fe^{2+}_{0.45})O_4$ with ~ 44 mole% ulvöspinel

129   (Fe_2TiO_4), 29% $FeCr_2O_4$, 15% Fe_3O_4, and 12% $MgAl_2O_4$.

130   In diffraction patterns, the occurrence of chenmingite is marked by disintegration of

131   the chromite grain into a highly textured aggregate of two spinel phases (based on lattice

132   parameters, chromite and an Fe-, Cr-rich ulvöspinel) with a grain size of roughly 50 nm.

133   Chenmingite diffraction implies a similar grain size but it exhibits less broad profiles than

134   nearby chromite and ulvöspinel and marked orientation. For structure refinement, we chose a

135   pattern from the border of the chromite grain near a shock melt pocket (Fig. 2). In this

136   pattern, chenmingite exhibits continuous Debye fringes with intensity variation along the

137   azimuthal angle, which we fitted with both March-Dollase and spherical harmonics.

138   Diffraction from surrounding chromite (around and underneath the lamella) could not be

139   completely avoided and this resulted in spotty broad Bragg reflections, which were initially

140   fitted by modeling a preferred orientation, followed by a Le Bail fit. |F(hkl)| of overlapping

141   reflections of chenmingite may have been compromised but this could not be avoided. For

142   chenmingite initially, the xieite structure was initially used as a model because we assumed

143   the diffraction patterns were generated by this phase. After Le Bail extraction of apparent

144   structure factor moduli, a reversed Monte Carlo optimization in space group $P1$ was

145   performed. The optimized structure was compatible with space group $Pnma$ but not $Cmcm$

146   (xieite) and exhibited a marked shift of one oxygen atom, consistent with a difference in

147   octahedral linkages relative to the xieite structure. The resulting structure was of the

148    $CaFe_2O_4$-type rather than the $CaTi_2O_4$-typeof xieite (Chen et al. 2003b, 2008). We obtained

149   an R_F of 28% for the initial xieite model and 11% for an optimized model in the $CaFe_2O_4$

150   harmunite-type structure. We also checked the modified CF-type structure (mCF) that had

151   been observed by Ishii et al. (2014) and found that R_F was nearly as high as that for xieite.

152   We repeated the Le Bail extraction based on a cell in space group $Pnma$ and conducted a

153   second reversed Monte Carlo optimization using a $CaFe_2O_4$-type model structure. This

154   second optimization resulted in an R_F of 9.1%. Le Bail-extraction converged to $R_p = 4.3%$

155   (Kraus and Nolze 1996). The difference between R_F and R_p reflects the noise level of the data

156   and overlap of chenmingite reflections with coexisting chromite. Rietveld refinement (von

157   Dreele and Larson 2004; Kraus and Nolze 1996) was then conducted based on the structure

158   model from the rMC optimization, and by either initially refining the preferred orientation

159   with the March-Dollase approach along 302 and 020 or by modeling texture with spherical

160   harmonics to 2nd order. Both approaches converged to the same orientation along the same

161   main directions. Subsequently, atomic positions and isotropic thermal displacement factors

162   were refined. The final wR_p of the Rietveld-refinement was 5.7% with a $\chi^2 = 43.9$ for 2062

163   observations. Pseudovoigt peak profiles were used with Gaussian terms U = 858, V = 231, W

164   = 17.1 and Lorentzian terms $L_x = 18.9$ and $L_y = 16.2$ (with GSAS).

165   We used the extracted structure factor moduli to obtain the average electron density at

166   each of the three cation sites. Site occupancies were assigned based on EPMA results and the

167   assessed relative average electron density of the cation sites. The relative electron density of

168   the three sites were assessed by rMC, using the Le Bail extracted structure factor moduli (the

169   multiplicity is taken into account by the rMC method and splitting of |F(hkl)| between strictly

170   overlapping hkl does not need to be considered here). rMC cannot directly assess partial

171   occupancies but electron density on distinct sites. Hence, we modeled a site with, for

172   example, ~ 20 electrons as 'Ca' in the rMC optimization (although there is no significant

173   concentration of Ca in the specimen). In reality, 20 electrons correspond to some occupancy

174   by the actually present species(e.g., 0.82·Cr + 0.18·Al or 0.69·Fe + 0.16·Al + 0.15·Mg, etc).

175   Using bulk composition as a constraint, we obtained the range of possible occupancies given

176   in Table 2. We repeated the procedure using different background- and orientation-fits prior

177   to Le Bail extraction. Resulting differences are within the given uncertainties. No potentials

178   were used in the rMC optimizations. We vary electron density at different sites by integers

179   changing the apparent cation (Ca = 20, Sc = 21 etc.). We interpolated if the best R_F was

180   obtained for an electron density intermediate between two integers. The sequence of electron

181   density for the three sites was reproducibly assessed as Site 3 > Site2 ≥ Site1. Form factors in

182   rMC are spherical. This is a sufficient approximation for the given data (with best $R_F = 9\%$.

183   Differences between spherical and higher order Bessel-function-based form factors are

184   generally not significant for $R_F > 2\%$). Isotropic thermal displacement factors of cation sites

185   were refined individually, and those of O were arbitrarily set equal to each other.

186   Synchrotron-diffraction data, which were obtained for regions free of xieite, reveal

187   that chenmingite has an orthorhombic *Pnma* CF-type structure with unit cell: $a = 9.715$ (6) Å,

188     $b = 2.87$ (1) Å, $c = 9.49$ (7) Å, $V = 264.6$ (4) Å, and $Z = 4$. Atom coordinates are given in

189   Table 2 and X-ray powder diffraction data are listed in Tables S1-S2. Chenmingite is isotypic

6

190   with harmunite ($CaFe_2O_4$). 50-60 vol% of the selected sample region were from chenmingite

191   and 40 - 50% from chromite and ulvöspinel (Fig. 2).

192

<div align="center">

DISCUSSION

</div>

194   Phase relations for $FeCr_2O_4$ (Ishii et al. 2014) show that chromite, the stable ambient

195   pressure phase in the spinel structure, breaks down to form ludwigite-type $Fe_2Cr_2O_5$ plus

196   eskolaite (Cr_2O_3) with increasing pressure (12-16 GPa, decreasing with increasing

197   temperature; see Fig. 3). At higher pressures (16-18 GPa), this phase assemblage yields to

198   single phase fields of chenmingite (CF-structured $FeCr_2O_4$) at lower temperature and xieite

199   (CT-structured $FeCr_2O_4$) at higher temperature. CF-type endmember $FeCr_2O_4$ undergoes a

200   transition upon release to ambient conditions (mCF; Ishii et al. 2014) whereas xieite can be

201   recovered to ambient conditions. Type chenmingite contains Mg and Al as minor components

202   and the formula may be broken down as approximately 75 mole% chenmingite, 15%

203    $MgAl_2O_4$, and 7% $MgCr_2O_4$. In the $MgCr_2O_4$ system, the CT structure is stable relative to CF

204   to low temperatures (< 1100°C; Ishii et al. 2015). For $MgAl_2O_4$, the CF-structure is stable

205   only above 23 GPa and 1600 ºC (Kojitani et al. 2007) up to at least 2000°C whereas the CT-

206   structured phase appears only above ~ 40 GPa (Ono et al. 2006; Ishii et al. 2015).

207   Disregarding real mixing volumes, an increasing $FeCr_2O_4$–component is expected to reduce

208   the pressure of the spinel-to-postspinel transformation, whereas the $MgAl_2O_4$ component

209   appears to stabilize the CF-over the modified CFstructue in the given $(Fe,Mg)(Cr,Al)_2O_4$

210   solid solution.

211   Comparing all examined end-member phase diagrams, the CF-structure (i.e.,

212   chenmingite) is the low-temperature, high-pressure form and the CT-structure (xieite) is the

213   high-temperature, high-pressure form. This experimental finding is consistent with the

214   observation of chenmingite as dominant over xieite in shocked chromite further away from

215   melt pockets.

216   The ratio of the sum of the lengths of the two long axes over that of the short axis

217   (a+c)/b (in standard cell setting) of 6.67 of type chenmingite is within the range of other CF-

218   type phases reported in the literature: 6.64 to 6.70 (Irifune et al.1991; Lazic et al. 2006;

219   Arevalo-Lopez et al. 2010; Ishii et al. 2018) including mCF-type $FeCr_2O_4$ (6.66; Ishii et al.

220   2014). Thus, the relative contraction of the c-axis of chenmingite is compensated by

221   expansion of the a- and b-axis. An apparent relation of the ratio of the effective cation radii

7

222   with this axial ratio is well matched by chenmingite. On the other hand, the apparent bond

223   valences are low, with values between 4 and 5 rather than 6. This observation suggests a high

224   degree of disorder of the anion lattice (because the relation between cation radii and cell-

225   parameters are well within the expected range). Such disorder is not unexpected in a

226   structure of limited metastability.

227   The EPMA analyses show no significant difference in chemistry between host

228   chromite and either xieite or chenmingite, which suggests that both chenmingite and

229   xieite formed by solid-state transformation from precursor chromite under high pressures

230   and temperatures during the Tissint impact event on Mars. These features are consistent

231   with expectations based on phase relations of the $FeCr_2O_4$ system (Fig. 3). Upon release

232   breakdown to eskolaite and Fe-Cr-ludwigite is not observed, consistent with rapid

233   temperature-release at still high dynamic stresses, which also allow for the conservation

234   of bridgmanite (Tschauner et al. 2014). Bridgmanite has been observed in shock melt

235   pockets of Tissint (Ma et al. 2016). It is important to note, in this context, that xieite

236   regions (aggregates of sub-micrometer-sized crystals) are always in contact with melt

237   pockets, whereas chenmingite lamellae only occur within the precursor chromite, a few

238   micrometers away from the melt pockets. This spatial correlation suggests that

239   chenmingite formed in the same pressure regime as xieite but at lower temperatures. A

240   similar textural relationship between xieite and chenmingite has been reported for the

241   Suizhou S6-L6-chondrite (Chen et al. 2003a).

242

243   **IMPLICATIONS**

244   In meteorites and, possibly, in terrestrial impactites, chenmingite and xietite document

245   the effect of high-pressure, high-temperature shock conditions on precursor chromite. Based

246   on the $FeCr_2O_4$ system, the formation of chenmingite from chromite requires pressures

247   exceeding 16-18 GPa and temperatures below ~1350°C. The formation of xieite requires

248   comparable pressures but higher temperatures. Peak shock pressures in Tissint have been

249   estimated to ~ 30 GPa (Baziotis et al. 2013; Walton et al. 2014; Ma et al. 2016). Generally,

250   kinetic phase boundaries are shifted relative to the thermodynamic ones to higher pressure at

251   lower temperature as evidenced by the zoned paragenesis strained olivine $\rightarrow$ ringwoodite or

252   ahrensite $\rightarrow$ wüstite + bridgmanite around Tissint shock-melt pockets (Ma et al. 2016).

253   Equivalently, chenmigite represents a cooler regime within a sequence of kinetically shifted

254 phase boundaries along a temperature gradient of a hotspot: Chromite with deformation

255 twinning $\rightarrow$ chenmingite $\rightarrow$ xieite. Hence, chenmingite and xieite are potential markers for

256 S4 to S6 level shock metamorphism depending on the approximate temperature regime of

257 formation. That is within or at some distance from a shock melt pocket or vein.

258   Chromite is commonly observed as an exsolution phase from former high-pressure

259 silicates in diamonds (e.g., Brenker et al. 2002). In the Earth's transition zone, Cr and Ti are

260 easily dissolved in majoritic garnet (Kessel et al. 2005) and may not be major constituents of

261 accessory minerals such as in spinel peridotite. On the other hand, an ilmenite-inclusion at a

262 remnant pressure of 10-12 GPa has been found in diamond (Tschauner et al. 2018). Hence,

263 the occurrence of chenmingite and xieite in adamantiferous metasomatized mantle appears

264 possible. Within such an environment, chenmingite or xieite could operate as carriers of high

265 field strength elements.

266

267

276

277 **REFERENCES**

278 Arevalo-Lopez, A.M., Dos santos-Garcia, A.J., Castillo-Martinez, E., Duran, A., and Alario-

279   Franco, M.A. (2010) Spinel to $CaFe_2O_4$ transformation: Mechanism and properties of β-

280     $CdCr_2O_4$. Inorganic Chemistry, 49, 2827–2833.

281 Armstrong, J.T. (1995) CITZAF: a package of correction programs for the quantitative

282   electron microbeam X-ray analysis of thick polished materials, thin films, and particles.

283   Microbeam Analysis, 4, 177–200.

284 Baziotis, I.P., Liu, Y., DeCarli, P.S., Melosh, H.J., McSween, H.Y., Bodnar, R.J., and Taylor,

285 L.A. (2013) The Tissint martian meteorite as evidence for the largest impact excavation.

286 Nature Communications, 4:1404/DOI:10.1038/ncomms2414, 7 pp.

287 Brenker, F.E., Stachel, T., and Harris, J.W. (2002) Exhumation of lower mantle inclusions in

288 diamond: ATEM investigation of retrograde phase transitions, reactions and exsolution.

289 Earth and Planetary Science Letters, 198, 1–9.

290 Chen, M., Shu, J., Mao, H.-K., Xie, X., and Hemley, R. (2003a) Natural occurrence and

291 synthesis of two new postspinel polymorphs of chromite. Proceedings of the National

292 Academy of Sciences, 100, 14651–14654.

293 Chen, M., Shu, J., Xie, X., and Mao, H.K. (2003b) Natural $CaTi_2O_4$-structured $FeCr_2O_4$

294 polymorph in the Suizhou meteorite and its significance in mantle mineralogy.

295 Geochimica et Cosmochimica Acta, 67, 3937–3942.

296 Chen, M., Shu, J., and Mao, H.K. (2008) Xieite, a new mineral of high-pressure $FeCr_2O_4$

297 polymorph. Chinese Science Bulletin, 53, 3341–3345.

298 Dera, P., Zhuravlev, K., Prakapenka, V., Rivers, M. L., Finkelstein, G. J., Grubor-Urosevic,

299 O., Tschauner, O., Clark, S. M., and Downs R. T. (2013) High pressure single-crystal

300 micro X-ray diffraction analysis with GSE_ADA/RSV software. High Pressure

301 Research, 33, Special Issue (SI), 466–484.

302 Irifune, T., Fujino, K., and Ohtani, E. (1991) A new high-pressure form of $MgAl_2O_4$. Nature,

303 349, 409–411.

304 Ishii, T., Kojitani, H., Tsukamoto, S., Fujino, K., Mori, D., Inaguma, Y., Tsujino, N.,

305 Yoshino, T., Yamazaki, D., Higo, Y., Funakoshi, K., and Akaogi, M. (2014) High-

306 pressure phase transitions in $FeCr_2O_4$ and structure analysis of new post-spinel $FeCr_2O_4$

307 and $Fe_2Cr_2O_5$ phases with meteoritical and petrological implications. American

308 Mineralogist, 99, 1788–1797.

309 Ishii, T., Kojitani, H., Fujino, K., Yusa,H., Mori, D., Inaguma,Y., Matsushita, Y., Yamaura,

310 K., and Akaogi, M. (2015) High-pressure high-temperature transitions in MgCr2O4 and

311 crystal structures of new $Mg_2Cr_2O_5$ and post-spinel $MgCr_2O_4$ phases with implications

312 for ultrahigh-pressure chromitites in ophiolites. American Mineralogist, 100, 59–65.

313 Ishii, T., Sakai, T., Kojitani, H., Mori, D., Inaguma, Y., Matsushita, Y., Yamaura, K.,

314 and Akaogi, M. (2018) High-pressure phase relations and crystal structures of postspinel

315   phases in MgV_2O_4, FeV_2O_4, and $MnCr_2O_4$: Crystal chemistry of AB_2O_4 postspinel

316   compounds. Inorganic Chemistry, 57, 6648–6657.

317   Kessel, R., Schmidt, M., Ulmer, P., and Pettke, T. (2005) Trace element signature of

318   subduction-zone fluids, melts and supercritical liquids at 120–180 km depth. Nature,

319   437, 724–727.

320   Kojitani, H., Hisatomi, R., and Akaogi, M. (2007) High-pressure phase relations and crystal

321   chemistry of calcium ferrite-type solid solutions in the system $MgAl_2O_4$-Mg_2SiO_4.

322   American Mineralogist, 92, 1112–1118.

323   Kraus, W. and Nolze, G. (1996) PowderCell – a program for the representation and

324   manipulation of crystal structures and calculation of the resulting X-ray powder patterns.

325   *Journal of* Applied Crystallography, 29, 301–303.

326   Lazic, B., Kahlenberg, V., J.Konzett, J., and Kaindl, R. (2006) On the polymorphism of

327     $CaAl_2O_4$-structural investigations of two high pressure modifications. Solid State

328   Sciences, 8, 589–597.

329   Ma, C. (2018) A closer look at shocked meteorites: Discovery of new high-pressure minerals.

330   American Mineralogist, 103, 1521–1522.

331   Ma, C. and Tschauner, O. (2017) Chenmingite, IMA 2017-036. CNMNC Newsletter No. 38,

332   August 2017, page 1037; Mineralogical Magazine, 81, 1033–1038.

333   Ma, C., Tschauner, O., Beckett, J.R., Liu, Y., Rossman, G.R., Zhuravlev, K., Prakapenka, V.,

334   Dera, P., and Taylor, L.A. (2015) Tissintite, $(Ca,Na,\square)AlSi_2O_6$, a highly-defective,

335   shock-induced, high-pressure clinopyroxene in the Tissint martian meteorite. Earth and

336   Planetary Science Letters, 422, 194–205.

337   Ma, C., Tschauner, O., Beckett, J.R., Liu, Y., Rossman, G.R., Sinogeikin, S.V., Smith, J.S.,

338   and Taylor, L.A. (2016) Ahrensite, γ-Fe_2SiO_4, a new shock-metamorphic mineral from

339   the Tissint meteorite: implications for the Tissint shock event on Mars. Geochimica et

340   Cosmochimica Acta, 184, 240–256.

341   Ma, C., Tschauner, O., Beckett, J.R., and Liu, Y. (2018) Discovery of chenmingite,

342     $FeCr_2O_4$ with an orthorhombic $CaFe_2O_4$-type structure, a shock-induced high-pressure

343   mineral in the Tissint martian meteorite. 49th Lunar and Planetary Science Conference,

344   Abstract #1564.

345   Prescher, C. and Prakapenka, V.B. (2015) DIOPTAS: a program for reduction of two-

346   dimensional X-ray diffraction data and data exploration. High Pressure Research, 35,

347   223–230.

348   Tschauner, O., Huang, S., Greenberg, E., Prakapenka, V.R., Ma, C., Rossman, G.R., Shen,

349   A.H., Zhang, D., Newville, M., Lanzirotti, A., and Tait, K. (2018) Ice-VII inclusions in

350   diamonds: Evidence for aqueous fluid in the Earth's deep mantle. Science, 359, 1136–

351   1139.

352   von Dreele, R.B. and Larson, A.C. (2004) General Structure Analysis System (GSAS). Los

353   Alamos National Laboratory Report LAUR, New Mexico.

354   Walton, E.L., Sharp, T.G., Hu, J., and Filiberto, J. (2014) Heterogeneous mineral

355   assemblages in martian meteorite Tissint as a result of a recent small impact event on

356   Mars. Geochimica et Cosmochimica Acta, 140, 334–348.

357
358
359
360
361

12

362   **Table 1**. EPMA data for type chenmingite and associated phases.

363

Constituent	chenmingite	xieite	chromite	Fe,Cr-rich ulvöspinel
wt%	n=15[a]	n=7	n=12	n=11
Cr_2O_3	57.5 (0.5)[b]	55.9 (0.6)	57.7 (0.4)	20 (2)
Al_2O_3	7.1 (0.1)	6.79 (0.05)	7.2 (0.2)	5.3 (0.4)
TiO_2	0.70 (0.05)	0.8 (0.1)	0.65 (0.03)	15.9 (0.6)
FeO	29 (1)	30.1 (0.7)	27.4 (0.9)	53 (2)
MgO	4 (1)	3.2 (0.2)	5.2 (0.6)	2.2 (0.2)
MnO	0.62 (0.03)	0.62 (0.01)	0.63 (0.03)	0.76 (0.03)
Total	98.9	97.4	98.8	97.2
No. O atoms	4	4	4	4
Cr	1.60	1.59	1.60	0.57
Al	0.29	0.29	0.30	0.23
Ti^{4+}	0.02	0.02	0.02	0.44
Fe^{3+} [c]	0.06	0.08	0.07	0.31
Fe^{2+} [c]	0.79	0.83	0.73	1.31
Mg	0.23	0.17	0.27	0.12
Mn	0.02	0.02	0.02	0.02
Sum cations	3.01	3.00	3.01	3.00

364   [a] n = number of analyses.
365   [b] Errors given inside parentheses are one standard deviation of the mean based on all of the
366   analyses.
367   [c] Fe^{3+} and Fe^{2+} were calculated from total Fe to produce the ideal M_3O_4 stoichiometry.
368

13

369 **Table 2**. Fractional atom coordinates, site fractional occupancies, and isotropic thermal
370 displacement factors of chenmingite. Site occupancies of O are fixed. All atoms reside on
371 Wyckoff sites 4c. Isotropic displacement parameters are in $Å^2$.
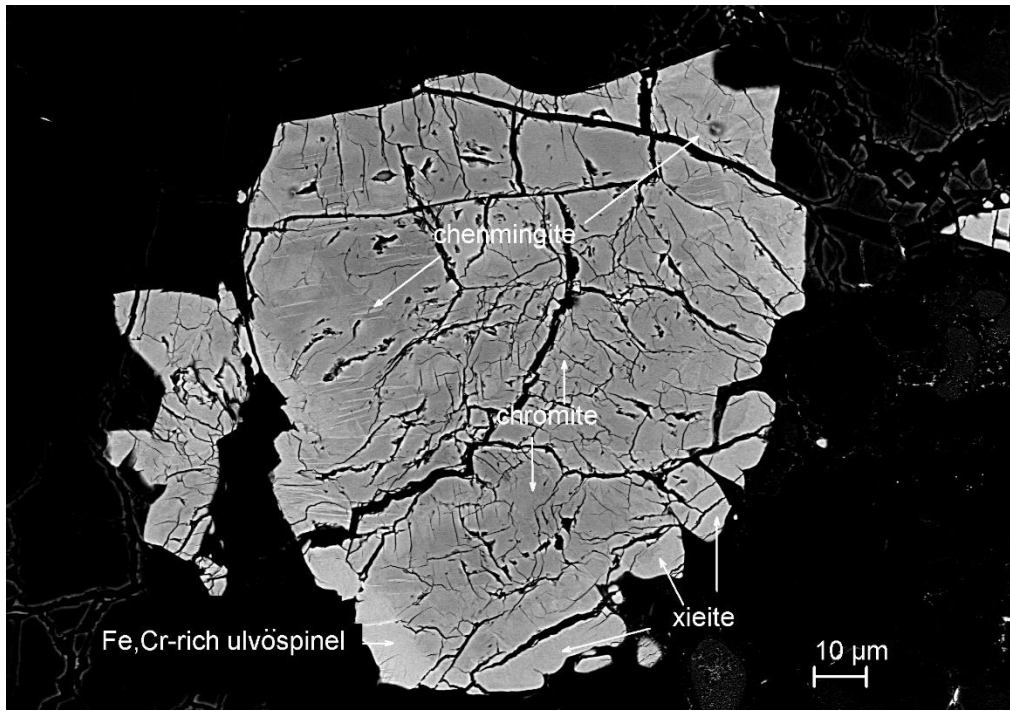
372

Atom	x	y	z	SOF	Uiso
Cr1	0.754(4)	0.25	0.347(2)	0.80(4)	0.040(8)
Al+Mg	0.754(4)	0.25	0.347(2)	0.20(4)	0.040(8)
Cr2	0.933(2)	0.25	0.102(9)	0.67(18)	0.011(8)
Al+Mg	0.933(2)	0.25	0.102(9)	0.29(7)	0.011(8)
Fe1	0.92(4)	0.25	0.61(2)	0.87(10)	0.048(1)
Cr3	0.92(4)	0.25	0.61(2)	0.13(10)	0.048(1)
O1	0.21(1)	0.25	0.84(2)	1	0.03(2)
O2	0.115(4)	0.25	0.52(1)	1	0.03(2)
O3	0.52(1)	0.25	0.21(7)	1	0.03(2)
O4	0.42(1)	0.25	0.58(1)	1	0.03(2)

373

374

14

375
376   (a)
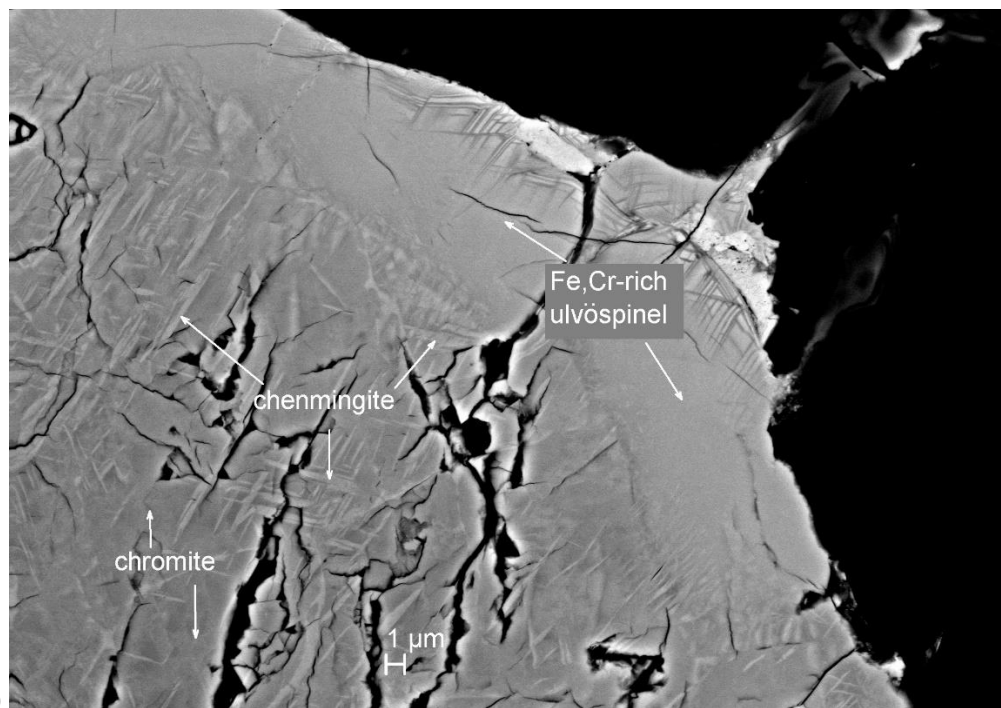

377   (b)
378

15
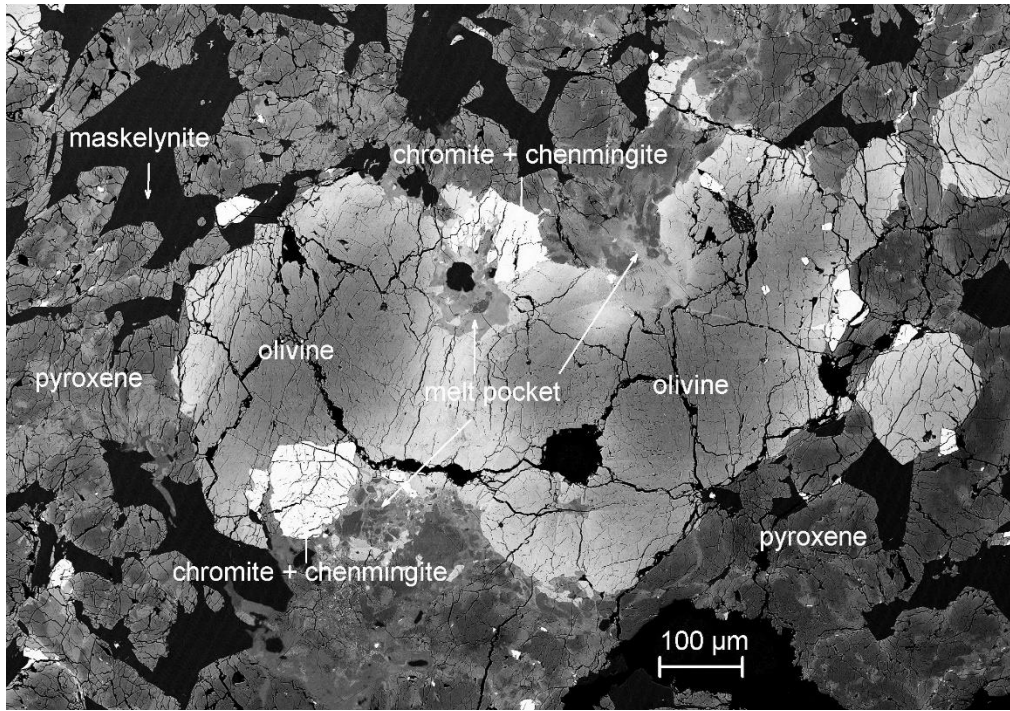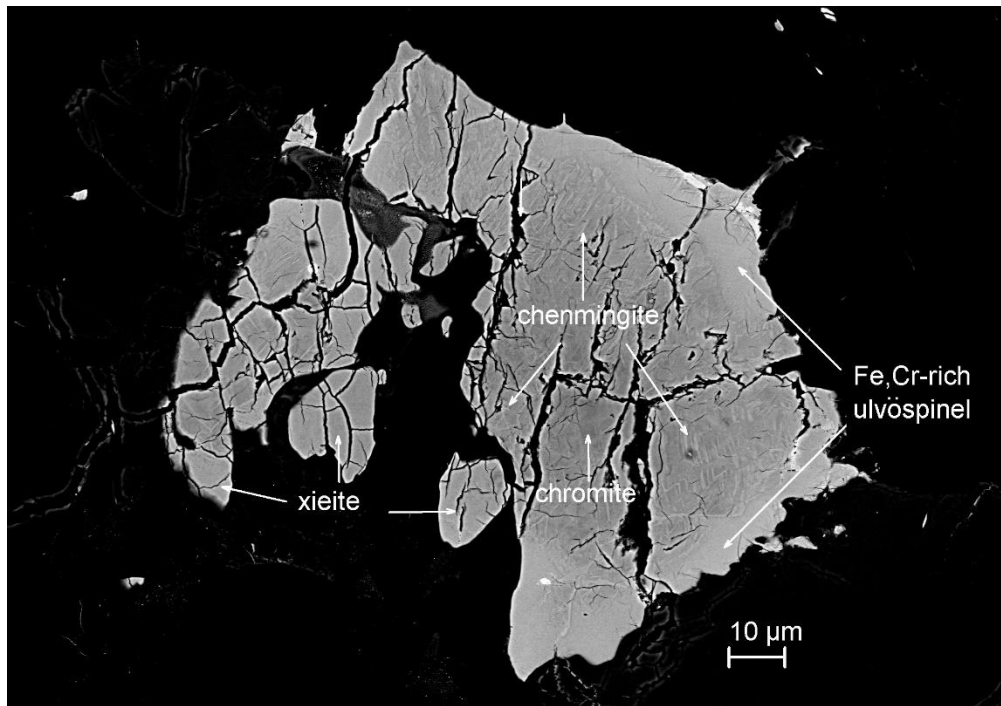
379   (c)

380   (d)

381   **Figure 1**. (a) Backscatter electron (BSE) image showing the chenmingite-bearing chromite
382   grains next to shock melt pockets in Tissint. (b)(c) Enlarged BSE images of areas in panel a
383   revealing chenmingite in two chromite grains with xieite and Fe,Cr-rich ulvöspinel. (d)
384   Enlarged BSE image of area in panel c showing chenmingite lamellae in chromite.
385

16
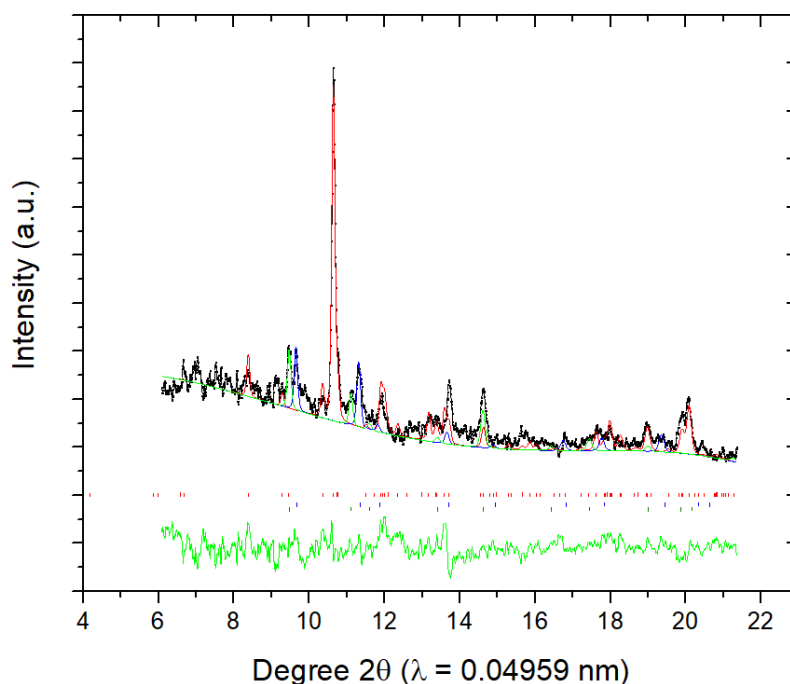
386
387 **Figure 2**. Polycrystalline diffraction pattern of chenmingite, chromite and ulvöspinel. red
388 line: Rietveld-refined modeled pattern of chenmingite, blue and green lines: Le-Bail fitted
389 patterns of chromite and ulvöspinel, black crosses: observed pattern, bottom green line:
390 residual of fit, red tick marks: allowed reflections of chenmingite. Blue and green tick marks:
391 chromite and ulvöspinel. The chenmingite aggregate is fine grained, powder-like but highly
392 oriented. Preferred orientation along axes 302 and 020 was modeled. Extracted structure
393 factor moduli were corrected for orientation effects. The primary beam wavelength was
394 0.4959 Å.
395

396
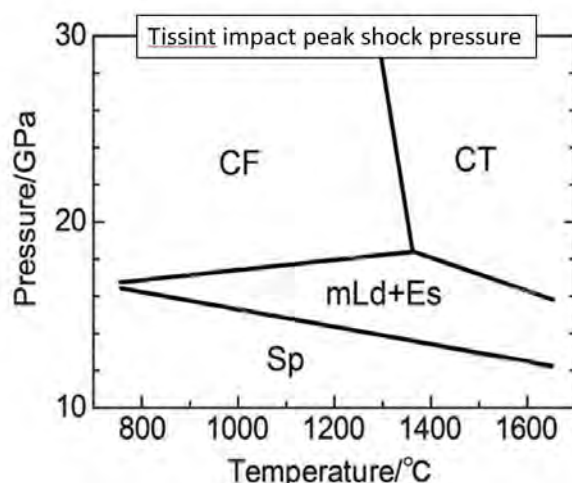
397 **Figure 3**. Phase diagram of $FeCr_2O_4$ based on Ishii et al. (2014). Sp: spinel-$FeCr_2O_4$
398 (chromite); mLd: modified ludwigite type $Fe_2Cr_2O_5$; Es: eskolaite; CF: CF-structured
399 $FeCr_2O_4$ (chenmingite); CT: CT-structured $FeCr_2O_4$ (xieite).

17